ACS APPLIED ELECTRONIC MATERIALS

pubs.acs.org/acsaelm Article

Breathable, Wireless, Thin-Film Wearable Biopatch Using Noise-Reduction Mechanisms

Nathan Rodeheaver, Hojoong Kim, Robert Herbert, Hojin Seo, and Woon-Hong Yeo*

Cite This: ACS Appl. Electron. Mater. 2022, 4, 503−512 Read Online

ACCESS | Metrics & More | Article Recommendations | Supporting Information

ABSTRACT: Skin-mounted wearable electronics are prone to motion artifacts from many sources, including sensor delamination, changes in electrode contact, skin strain, device movement, and changes in skin hydration. There continues to be increased development of wearable electronics that enable continuous physiological monitoring throughout daily life. However, these devices often fail to record accurate signals during movement such as bending, lifting, and stretching. Motion artifacts are also intensified during prolonged and repeated use from factors like decreased adhesion by sweating or dust. Here, we introduce a breathable, wireless wearable biopatch using an enhanced noise-reduction mechanism. The air-permeable, strain-isolated design is developed through computational modeling and experimental study and validated with human subjects during daily activities and exercise. The soft, lightweight wearable device is made with a breathable elastomeric membrane and stretchable thin-film connectors. The skin-like biopatch has a smaller form factor than comparable commercial health monitors while maintaining intimate contact without the need for adhesives or straps. In addition, we demonstrate superior sweat-wicking and skin temperature regulation with a reusable elastomer substrate. Together, this design can manage device movement, reduce skin strain, decrease electrostatic noise, and remove sweat to provide high-quality, real-time, continuous electrocardiogram recordings without data loss.

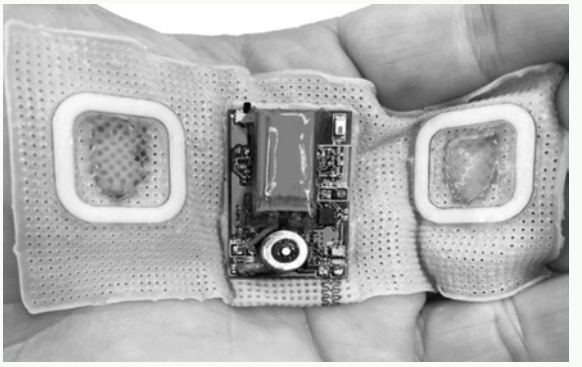

KEYWORDS: *breathable biopatch, wearable electronics, soft system, health monitor, noise reduction*

INTRODUCTION

The development of wearable electronics continues to outpace the growth of electronics in general with a compound annual growth rate of 15.5% compared to 6%.[1,2] The benefit and application of smaller, lighter, wireless devices for healthcare monitoring are clear for both healthcare providers and patients. Within the past year, the US Food & Drug Administration has issued emergency use authorization for six remote or wearable patient monitoring devices to help reduce healthcare provider exposure during the COVID-19 pandemic.[3] All of this development, and especially emergency use, has raised concerns[4] over safety for patients as the world transitions to more virtual healthcare. Particularly, at-home devices are known to report inaccurate measurements, which can be dangerous when diagnosing life-threatening arrhythmias.[4] It is extremely important to develop devices capable of measuring accurate signals. Improving signal measurement starts with a better design of sensors and devices. Noise can come from many different sources. Some prior works have focused on matching and emulating the properties of skin.[5−8] This allows the device to move with the skin, reducing the relative motion between the skin contact and the sensor. Others have used intrinsically sensitive and flexible materials to improve signal quality and sensor response.[9,10] As wearable devices improve, we continue to use them in more stressful situations. This is a critical part of design and development. Sensors developed in the lab must be tested in real-world situations. One of the ironic signs of progress is that wearable devices have noisy data. This is directly related to the tremendous strides that have been made to miniaturize and mobilize physiological monitoring devices. In the past, a healthcare provider required that the subject remain completely stationary during data collection. Now, wearable devices are used at home by untrained people. This presents challenges of improper placement or inconsistent skin conditions between subjects. However, it also provides an excellent opportunity for researchers to meet these challenges with improved designs that produce consistent and reliable data. The next step is to identify meaningful ways to improve signal quality.

Wearable devices are affected by a wide range of motions and are mounted to human skin, a dynamic, unstable,

Received: November 8, 2021
Accepted: January 5, 2022
Published: January 12, 2022

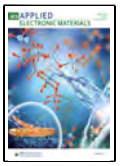

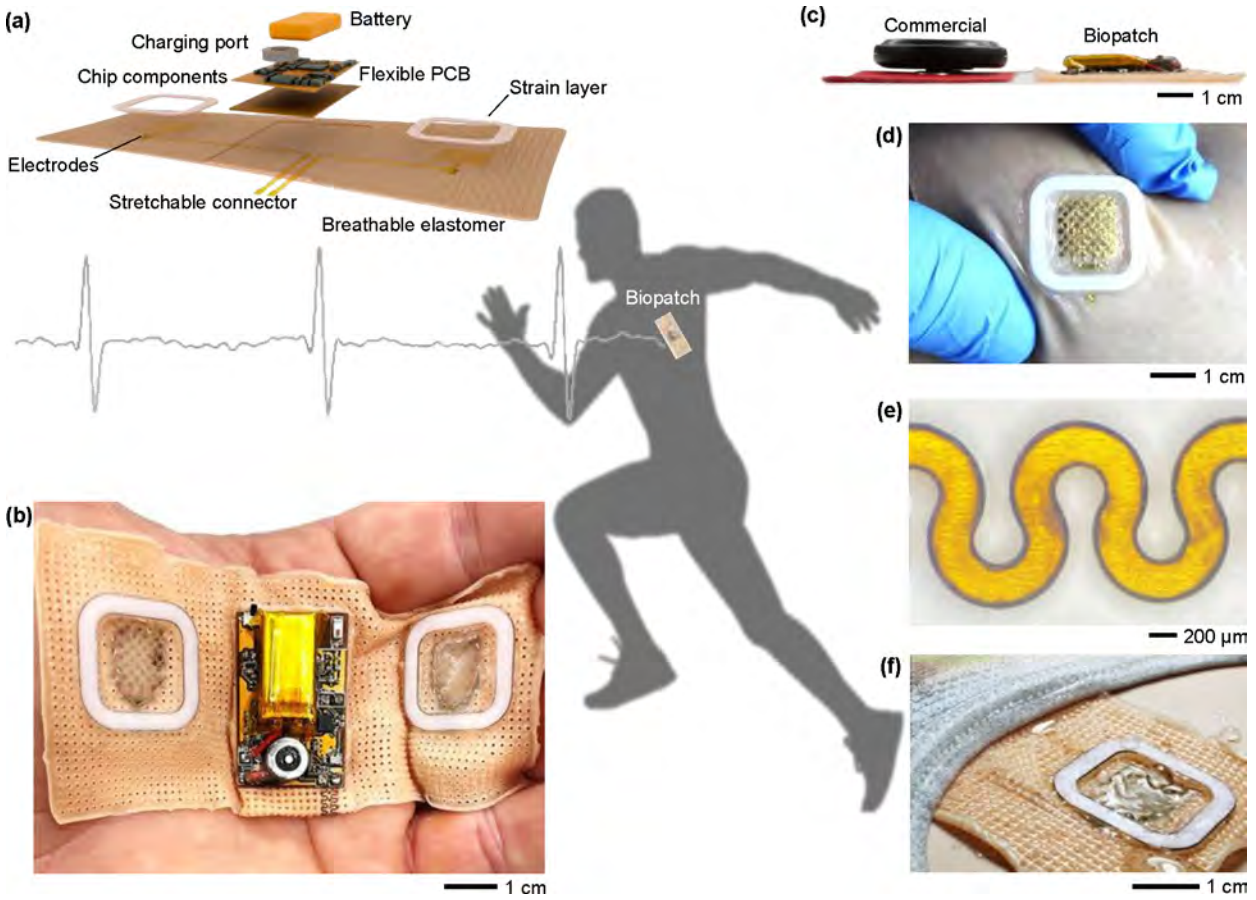

Figure 1. Overview of the device design and key components for noise reduction in the monitoring of ECG data. (a) Schematic illustration showing all components of a wearable biopatch. (b) Photo of a fabricated biopatch that is soft, flexible, and stretchable. (c) Comparison of a form factor between a commercial wearable health monitor and biopatch in part b. (d) Strain-isolating layer, surrounding the electrode, to avoid electrode deformation and sliding from external strain. (e) Thin-film connector, capable of 100% strain with negligible electrostatic noise. (f) Sweat-resistant, breathable elastomer to maintain stable skin hydration and reduce device delamination.

nonlinear material. The response of human skin is frequency dependent, with chaotic wave attenuation on the surface and shear waves traveling beneath in the dermis.[11−14] It is possible to measure the range of motions, such as maximum strain or shear, which can be used to design a device for withstanding these forces. Device stability and improved signals have been shown with the use of soft materials that conform better to the skin.[15−18] Skin strain and vibration also disrupt the skin's half-cell potential[19] and the contact of the electrodes with the skin. Prior works have shown signal improvement from stretchable thin-film electrodes[20−24] and demonstrated that stretchable electronics typically suffer connection problems from thin-film delamination during repeated strain.[11,25,26] In addition, during the device wearing, sweat causes fluctuations in electrocardiogram (ECG) recordings for gel electrodes[27] and also produces significant adhesion issues for dry electrodes which are commonly secured using straps.[28−30] There is a continued need for breathable materials that do not rely on adhesives or gels, which damage the skin over repeated or prolonged use.[31−35] Altogether, wearable devices need to mitigate the challenges of movement relative to the skin, changing electrode contact, insulation breakdown, and fluctuating skin hydration and sweat to record accurate signals. Our prior research introduced a strain isolation concept for motion artifact (MA) reduction, which still possesses issues of a merely flexible interconnector and rigidity from thick strain films.[36]

Here, we introduce an enhanced wearable system with a noise-reduction mechanism, demonstrating an enhanced signal-to-noise ratio as a long-term usable ECG monitor. An overview of the skin-friendly, wireless device is presented with examples of common sources of MAs. The methods for reducing the noise in each category are shared in greater detail, starting with the device size and form factor. Further progress of strain isolation design is described and studied with finite element analysis. We compare the performance of commonly used flexible connectors to new stretchable connectors. Finally, breathability testing and elastomer redesign show superior performance compared to commercially available devices and prior research.

RESULTS AND DISCUSSION

Overview of the Device Design and Noise-Reduction Mechanisms. Figure 1 captures the overview of the soft wireless biopatch with noise-reduction components. The ECG device that makes intimate contact with the skin uses stretchable, soft materials to bond with the skin. When placed on the chest, the biopatch wirelessly records ECG data and transmits it to the user's phone or tablet for signal analysis and long-term storage. Figure 1a shows a schematic diagram of the multilayered, integrated device design. Mesh electrodes are mounted on a perforated breathable elastomer layer and connected to the circuit using stretchable connectors. The

https://doi.org/10.1021/acsaelm.1c01107
ACS Appl. Electron. Mater. 2022, 4, 503−512

Table 1. Comparison of Form Factors of Recent Wearable ECG Monitors

reference	device name	form factor (mh/lw)	size (mm)			mass (g)
			l	w	h	
this work	Biopatch	0.0104	100	45	7.1	6.6
40	VSMS[a]	0.0225	140	130	18	22.8
36	SIS	0.0320	100	45	11	13.1
30	MAX-ECG[a]	0.0410	130	51	10	27.2
41	Zio-XT[a]	0.0492	127	51	13	24.5
42	MiCor A100[a]	0.2837	45.6	21.4	11.3	24.5

[a]Commercial devices.

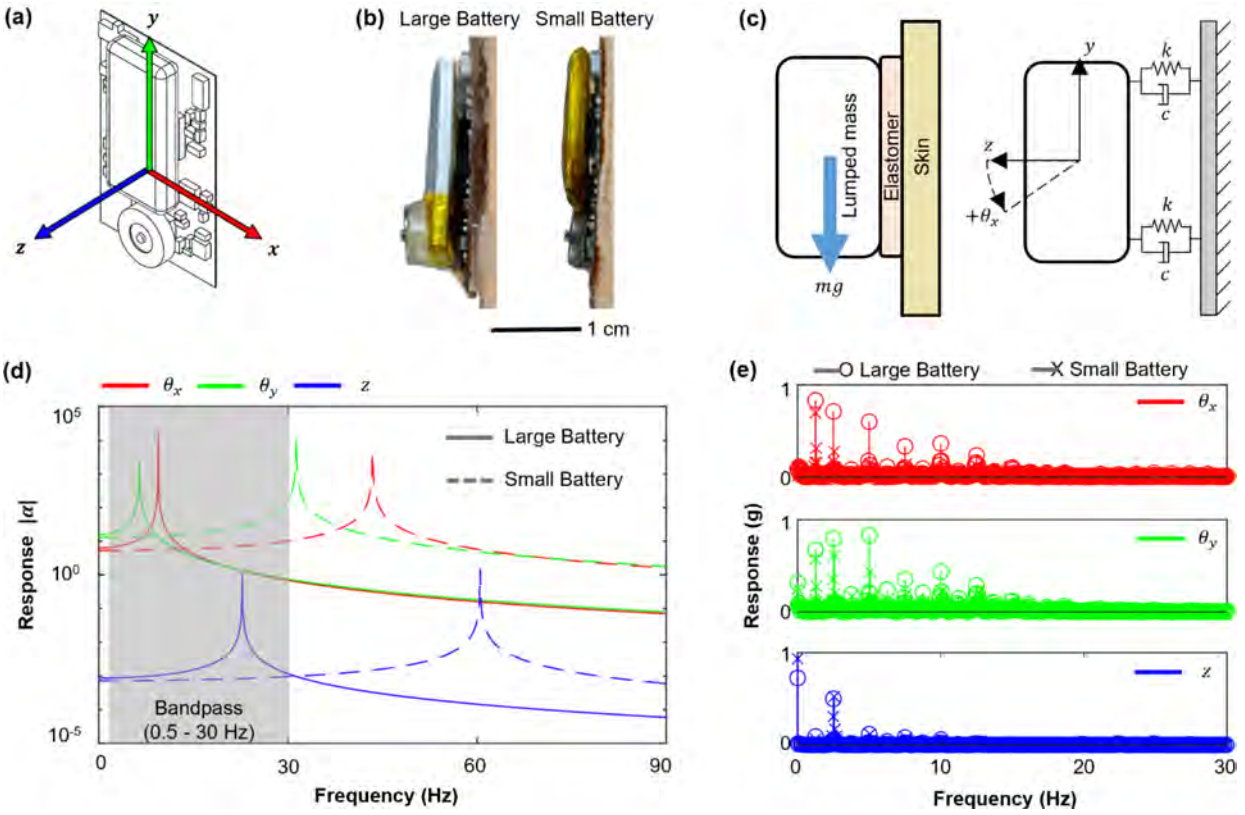

Figure 2. Device size and form factor considerations. (a) ECG device with large battery overlaid with coordinates aligned with the onboard accelerometer. (b) Side view of the device for a large battery (2.59 g, 28 × 14 × 3.5 mm^3) and a small battery (1.13 g, 22 × 11 × 3 mm^3). (c) Schematic diagram of the side view showing the lumped mass, elastomer, and skin with net acceleration acting through center of mass (left); free-body diagram of the yz-plane with elastomer and skin modeled as a spring−mass−damper system (right). (d) Three degree of freedom (3DOF) frequency response for x-rotation, y-rotation, and z-directions. Dashed lines show the response of the small battery design is tuned outside the bandpass filter for the ECG signal. (e) Fourier transform of accelerometer data for 3DOF modeled in part d. The large battery design shows additional motion at jogging frequency and harmonics for x-rotation and y-rotation.

wireless circuit is built using standard chip components on a flexible printed circuit board (fPCB). A lightweight, rechargeable battery (3.7 V, 40 mAh, 1.13 g) powers the device for over 8 h of continuous use and is recharged with a magnetic charging port. The strain-isolation layer (SIL) is mounted on the top side of the elastomer to surround the electrodes and control the movement or deformation of the electrodes. Pictures of the assembly process, device placement, and comparison with previous versions are shown in Supporting Information Figure S1. We used four main strategies to reduce noise in the measured ECG signals. The first was to lower the weight and thickness to reduce inertia effects from mass and maximize stability against vibration or delamination (Figure 1b). This advantage was achieved by using a smaller battery, thinner elastomer layers, and a thinner fPCB (Figure 1c). The result is a small footprint, with a smaller height than other comparable ECG patch devices (Table 1). The second strategy used strain isolation to limit electrode buckling, sliding, and damage. We tested different materials and developed an improved SIL with a smaller area that controlled electrode strain better (Figure 1d). Third, the global strain of the device and pressure on the connectors themselves proved to add noise in previous recording sessions, so additional insulation was added to the connectors to reduce electrostatic noise (Figure 1e). A breathable elastomer layer was used to eliminate fluctuations in contact impedance due to sweating (Figure 1f). Table S1 compares the effectiveness of these MA reduction strategies with different activities. A real-time demonstration of MAs from disturbance to the circuit, electrodes, and flexible connectors can be seen in Movie S1.

https://doi.org/10.1021/acsaelm.1c01107
ACS Appl. Electron. Mater. 2022, 4, 503−512

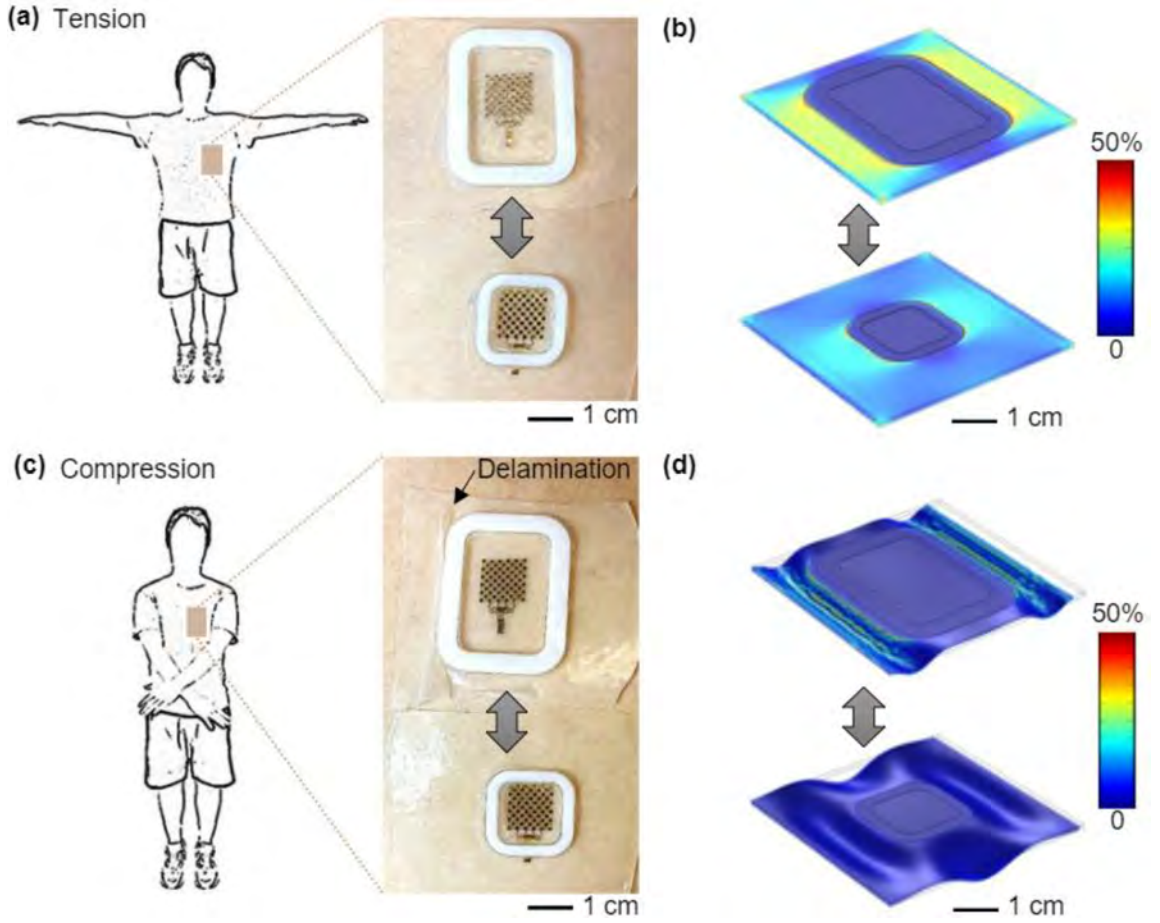

Figure 3. Validation of strain isolation via a comparison between large and small SIL under two loading conditions. (a) A case when arms are stretched, causing tension on the chest. The photo shows both SILs maintaining contact. (b) FEA shows a higher strain surrounding the large SIL. (c) A case when arms are crossed, causing compression on the chest. The photo shows delamination along the edge of the large SIL (top), while the small SIL maintains intimate contact. (d) FEA validates the most significant strain concentration on the large SIL (top), compared to the minimal deformation for the small SIL (bottom).

Consideration of Device Form Factor. Miniaturization of electronics has enabled more precise signal measurement in many fields of study, including biosignals for healthcare. The convenience and user preference of an ECG patch are easy to recognize when wearing bulky, conventional devices with multiple wires and straps. However, beyond convenience and comfort, this work shows that the small form factor is a critical design criterion to eliminate MAs from ECG signals beyond convenience and comfort. The form factor is defined here as the ratio of the height or thickness of a feature compared to its base area. For the same size footprint, a thicker device has a higher form factor. Table 1 also includes the form factor multiplied by the device mass, which is more comparable to the inertial properties of the system. We started by modeling the bulkiest part of the device, the circuit, and the battery to quantify the improvement. Figure 2a shows the major circuit components with the *XYZ* orientation of the onboard accelerometer. Previous versions used a larger battery and had pieces stacked on top of each other, while the new device was redesigned to keep the mass as close to the fPCB as possible (Figure 2b). We reduced power consumption for a smaller battery, resulting in a smaller form factor. A larger mass will be less stable from the effects of gravity acting through the center of mass, but vibrational modes amplify movement. Figure 2c shows the side view idealized circuit as a rectangular mass supported by an elastomer layer and the skin. This design is simplified for vibrational analysis to a rectangular mass supported by springs and dampers at each edge. This arrangement allows for three degrees of freedom: rotation about the *x*-axis, rotation about the *y*-axis, and linear movement along the *z*-axis. When a net acceleration moves the circuit relative to its anchoring point on the chest, the movement creates global stretching throughout the device, which causes MAs from stretching connectors and tugging at the electrodes. A full description of the modeling with boundary conditions, assumptions, and equations of motion is found in the Experimental Section and Supporting Information Figure S2. As summarized in Figure 2d, we modeled the vibrational response for the large and small battery designs. The large battery device (13.1 g) contains resonant frequencies within the range of ECG measurement. The resonant frequencies of the small battery device (6.6 g) are above 30 Hz. The signal noise induced by motion above 30 Hz is filtered out during post-processing. Additionally, jogging and other typical motions occur at frequencies below 10 Hz. Therefore, the larger battery device is prone to a more significant response when the driving frequency is close to its resonant frequency. This calculation is confirmed experimentally in Figure 2e where larger amplitudes are shown in *x* and *y* rotation for the large battery device. The devices were tested

https://doi.org/10.1021/acsaelm.1c01107
ACS Appl. Electron. Mater. 2022, 4, 503−512

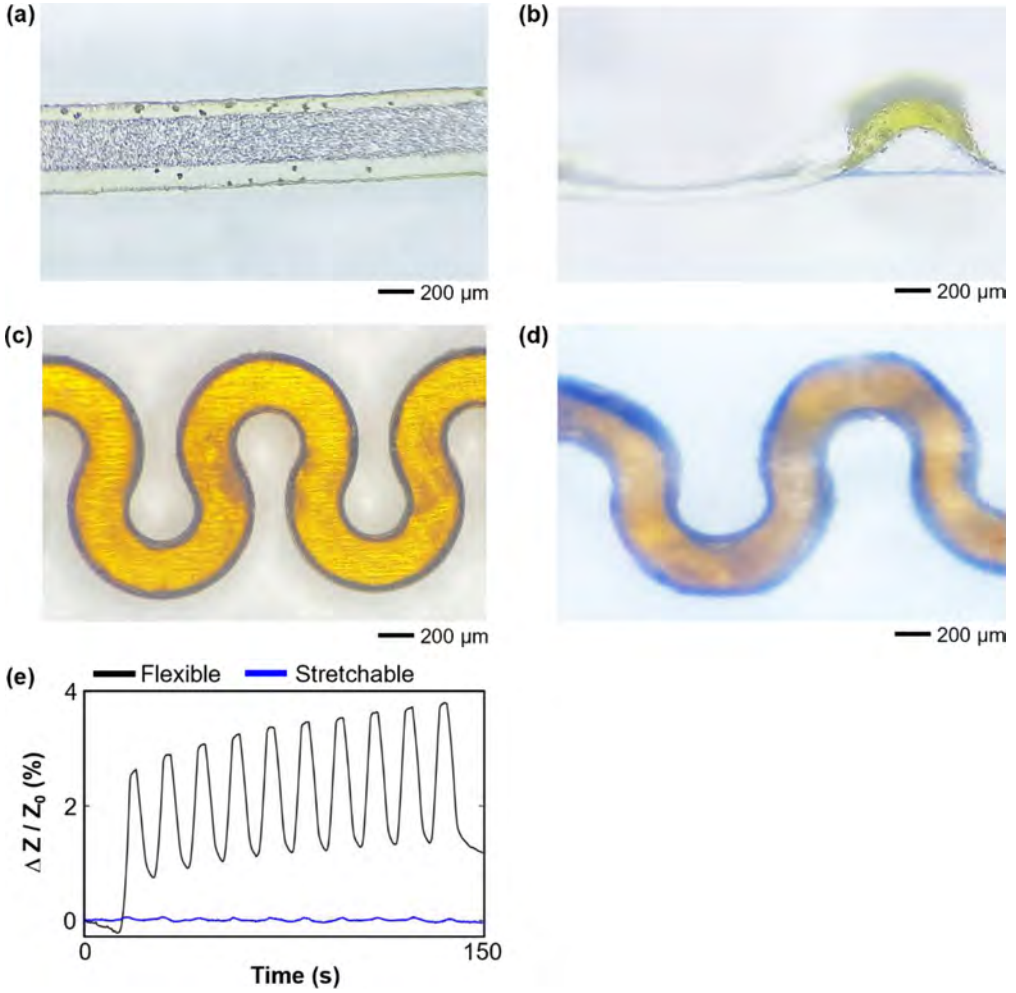

Figure 4. Performance comparison between a conventional flexible cable and a fabricated stretchable connector. (a) A conventional flexible cable for wearable devices. (b) Generated air gap from stretching, between the connector and elastomer; repeated stretching causes friction-induced electrostatic noise. (c) A fabricated membrane stretchable connector. (d) No adverse effect on the connector with repeated stretching. (e) Comparison of impedance values of two connectors during a cyclic stretch test. The flexible cable experiences a significant impedance change, while the stretchable connector has a negligible effect.

on the same subject during consecutive jogging sessions on a closed track. The primary jogging impact of 2.55 Hz can be seen in the z data. Together with the half-harmonic and following four harmonics, these are the dominant features seen in the plot (1.25, 2.55, 5, 7.5, 10, and 12.5 Hz). Both devices have a large amplitude response near the driving frequency of 2.55 Hz, but the small battery device does not contain the same rotational movement near 10 Hz. The entire system, including the human body and skin response, is more complex, but this data shows that form factor design considerations help contribute to the signal quality.

Validation of Strain Isolation with Different SIL Designs. Our previous work[36] showed that skin strain causes MAs by disturbing the contact impedance between the electrode and the skin. The SIL successfully shielded the electrode and surrounding skin, producing better ECG signals throughout jogging and other activities. We improved the design further by experimenting with additional materials and geometries. Mylar sheet was selected as a replacement for polyethylene because of its similar modulus and better resistance to solvents. Mylar is also able to be laser-cut, allowing for higher precision and faster prototyping of different sizes. Figure 3 shows the performance of two versions of the mylar SIL for two common body movements with each case compared to finite element analysis (FEA). Figure 3a represents an example when the subjects' arms are outstretched, causing tension on the skin and device. Figure 3b summarizes FEA results showing a strain distribution with tension on the SIL. The effectiveness of the SIL is shown by the strain reduction inside where the electrode is located. For each design, the elastomer stretches outside the SIL but is restricted inside the perimeter of the SIL. This restriction prevents electrode deformation while simultaneously maintaining conformal contact to the skin. The top design is surrounded by an area of larger strain (yellow portion). This area of strain concentration is more likely to delaminate from the skin. Figure 3c shows a case when the subjects' arms are crossed, causing compression and delamination at the edge of the SIL. The FEA results are shown in Figure 3d, with buckling that matches the delamination. The top SIL in each example has identical dimensions to the previous polyethylene version, while the bottom SIL is just large enough to surround the electrode pads in contact with the skin. The previous version surrounded the electrode by at least 5 mm on all sides. Through parametric study, we found that smaller SIL also reduced skin strain at the electrode. In fact, the smaller SIL

https://doi.org/10.1021/acsaelm.1c01107
ACS Appl. Electron. Mater. 2022, 4, 503−512

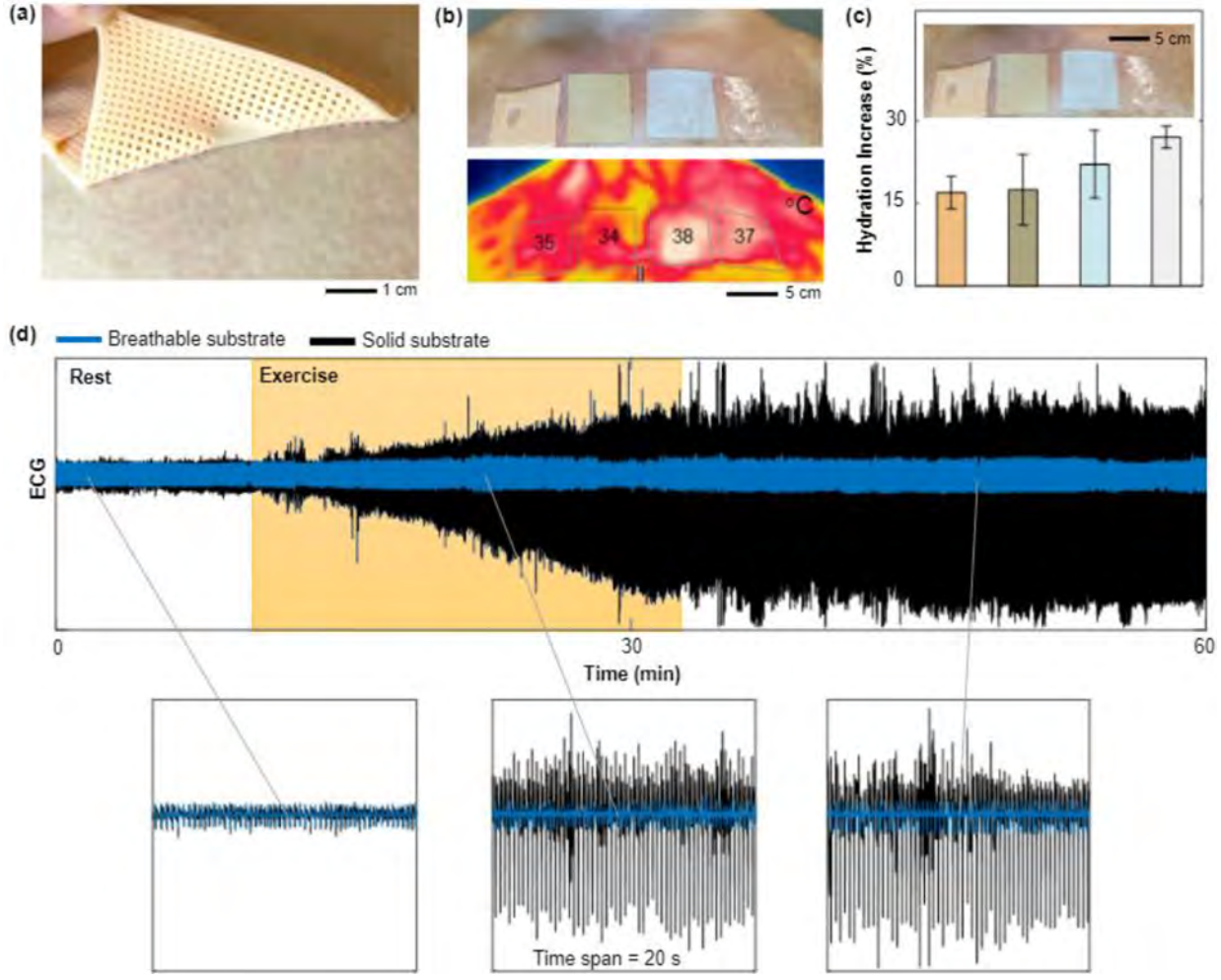

Figure 5. Demonstration of a breathable elastomer substrate. (a) Breathable elastomer with 500 mm perforations to wick sweat and water vapor from the skin. (b) Comparison of four types of substrates mounted on the chest: from left to right - breathable elastomer, medical tape 9907T (3M), micropore film (3M), and solid elastomer. The bottom image of the thermograph captures the temperature difference between substrates after exercise. (c) Percent increase of skin hydration according to substrate type. (d) Comparison of measured ECG data between the breathable substrate and the solid substrate. Even with exercises, the breathable membrane offers skin conformal, intimate contact of sensors to the skin, while a typical solid film shows a delamination issue due to excessive sweating. Callout plots show 20 s intervals of rest, exercise, and post-exercise.

design reduces the strain on the surrounding elastomer better than the large design. Both designs limit the strain at the electrode to less than 2%, but the small design also has less strain concentration surrounding the electrode. This arrangement reduces the chance of delamination by restricting a smaller area of skin, which is clearly seen in the case of tension (Figure 3b), with the prominent yellow portion. The observed delamination in Figure 3c corresponds with the expected FEA results (Figure 3d), showing increased strain concentrations and buckling at the interface of the elastomer and SIL. Additional pictures comparing each SIL for different arm movements can be seen in Figure S3. Movie S2 shows the real-time comparison between the two SILs, with separate trials where the location of each has been switched. In both cases, the small SIL outperforms the larger SIL by showing less delamination from the skin. We also observed the likelihood of delamination after repeated movements. Delamination was more likely when subjects performed arm-stretching movements in a sequence of tension and compression, compared to any individual movement. A sequence of movements is more realistic for replicating long-term monitoring and underscores the importance that wearable devices be designed to move with the body the entire time while being worn. The device stretch test results, material testing methods, SIL geometry calculations, and FEA parameters are described in the Experimental Section and Supporting Information Figures S4 and S5.

Performance Comparison between a Flexible Cable and a Stretchable Connector. Our prior work demonstrated the superior performance of a soft sensor system to bulkier devices with wires.[36] The longer a wired connector, the more chance of strain within the connector or tugging and pulling at the electrodes. During continuous ECG monitoring with the wireless device, we observed other MA noise even with the strain reduction method of the SIL. We identified spikes in the measured ECG signals when pressing on the connectors between the circuit and electrodes (Figure 1a). Even when the electrodes were isolated, the movement of the circuit and stretching of connectors still produced MAs. Figure 4a shows a commonly used connector using a flexible thin film for the integrated wearable device. The conductive film sits on a polymer substrate for stability, but the top layer is uninsulated and open to the environment. An elastomeric material (EcoFlex 00-30, Smooth-On) has been used to

https://doi.org/10.1021/acsaelm.1c01107
ACS Appl. Electron. Mater. 2022, 4, 503−512

encapsulate connectors and doubles as an insulator. For minor strains, the elastomer provides adequate insulation. However, we observed delamination of the elastomer from the connection when samples are stretched up to 100%, which is caused by an air gap (Figure 4b) when the samples are released. Any subsequent stretching results in sliding between the flexible film connector and the elastomer. In contrast, a fabricated stretchable connector, shown in Figure 4c, can stretch with the elastomer (Figure 4d). We compared the performance of the flexible film connector to the stretchable connector during a stretch test. All samples were encapsulated with elastomer and clamped on either end to restrict movement at the measurement locations. Figure 4e shows the results of the change in impedance versus the displacement throughout 10 cycles of stretching. These values are with respect to the initial impedance value for each sample. The maximum value for the flexible film connectors is 3.81 and 0.0634% for stretchable connectors. The flexible cables show a growing change each cycle from yielding as well as elastomer delamination and sliding. The stretchable samples have a much smaller impedance change. This method using a stretchable connector helps reduce MA noise during movements that stretch the entire device. Details of the elastomer stretch test and fabrication of the stretchable connectors are provided in the Experimental Section and Supporting Information Figures S6 and S7.

Demonstration of a Breathable Elastomer Substrate. Breathability is one of the most critical factors to ensure long-term, continuous ECG recording. Skin hydration can fluctuate throughout the day, especially if the user exercises or is outside during hot, humid weather. Even in moderate temperature, excessive sweat can build up between the skin and elastomer, in the same way as when wearing medical gloves. Additionally, sweating increases the likelihood of skin irritation. Biocompatibility is also extremely important for long-term monitoring. For consistent signal quality, the device needs to be worn in the same place repeatedly. Skin irritation after repeated use can severely limit data collection. We used silicone elastomers that are certified skin-safe (Smooth-On), but these materials are not inherently breathable. To overcome this challenge, we developed a breathable elastomer substrate with holes that allow sweat to pass through (Figure 5a). We compared the breathable elastomer with two commercial tapes and solid elastomer. Figure 5b shows the samples' placement on the chest and a thermal image after the subject exercised for 20 min. The breathable elastomer had a temperature of 35 °C, performing similarly to the medical tape (3M, 9907T) with a temperature of 34 °C. The highest temperature recorded was 38 °C for micropore film (3M), and the solid elastomer was next highest at 37 °C. These results match the skin hydration data, shown in Figure 5c, where the percent increase of skin hydration is plotted for each sample with respect to the skin hydration measured directly above the sample. We expect an increase in skin hydration for an area of skin covered by any type of substrate. The breathable elastomer and the medical tape (9907T) again performed similarly with a 17% increase. The micropore film had a 22% increase, and the solid elastomer had a 27% increase. These values are consistent with the observed sweat on the skin immediately upon the removal of the tape when testing skin hydration, shown in Figure S8, as well as the water transmission comparison in Movie S3 between various substrates. The more breathable samples had lower skin temperatures and less change in skin hydration. The ultimate test, however, is the measured ECG signal. We tested the breathable and solid elastomer substrates, shown in Figure 5d. Both trials contained a rest period to establish a reference signal amplitude, followed by 30 min of exercise and an additional rest period. The breathable substrate maintains consistent signal amplitude throughout the exercise period with few MAs. The solid substrate has an increase in amplitude during exercise from the increase in hydration. Although this creates a more defined signal, the sweat also reduces adhesion, making the device more prone to MAs. These MAs can be seen during the period of exercise and the following rest (Figure 5d, lower inset) as the short-term spikes in signal amplitude. Additional photos of sweat mitigation from multiple subjects, details of the microneedle mold used for fabrication, and breathability vs substrate thickness are provided in the Experimental Section and Supporting Information Figure S9.

CONCLUSIONS

This paper reports a new class of wearable ECG monitors with noise-reduction mechanisms using the SIL, stretchable connectors, and breathable substrates. A comprehensive study using analytical, computational, and experimental methods defines common noise sources in ambulatory ECG recording and describes practical designs to improve signal quality. Smaller form factors and light weight are shown to reduce device movement while enhancing bonding with the skin. Skin strain is controlled at the electrode using smaller strain isolation layers that are less prone to delamination. Breathable elastomer substrates allow skin-friendly adhesion and outperform sweat and water vapor transmission compared to solid elastomer and commercial tapes. Stretchable connectors maintain low impedance change during excessive and repeated stretching. Collectively, the device design strategies presented in this work will help develop other wearable health-monitoring electronics for targeting ambulatory, real-time, continuous data recording of users in daily activities.

EXPERIMENTAL SECTION

Equations of Motion. We used a 3-degree-of-freedom model to characterize the dynamic and vibrational response of the circuit. The equations of motion are found by solving the force and acceleration relationships from the free-body diagrams in Figure S2. In symbolic matrix form, they are[37]

$$[M]\{\ddot{x}\} + [K]\{x\} = \{F\}$$

where $[M]$ and $[K]$ are the mass and spring matrices and $\{\ddot{x}\}$,$\{x\}$, and $\{F\}$ are the acceleration, displacement, and external force vectors. To find the resonant frequencies, we solve the eigenvalue problem by setting the force equal to zero. The simplified expanded form is given by

$$\begin{bmatrix} I_{xx} & 0 & 0 \\ 0 & I_{yy} & 0 \\ 0 & 0 & m \end{bmatrix} \begin{Bmatrix} \ddot{\theta}_x \\ \ddot{\theta}_y \\ \ddot{z} \end{Bmatrix} + \begin{bmatrix} (1/2)kb^2 & 0 & 0 \\ 0 & (1/2)ka^2 & 0 \\ 0 & 0 & 4k \end{bmatrix} \begin{Bmatrix} \theta_x \\ \theta_y \\ z \end{Bmatrix} = \begin{Bmatrix} 0 \\ 0 \\ 0 \end{Bmatrix}$$

where I_{xx} and I_{yy} are the respective rotation inertial properties of the entire system, m is the equivalent mass of the system, which corresponds to the directional acceleration terms ($\ddot{\theta}_x$, $\ddot{\theta}_y$, $\ddot{z}$), k is the equivalent spring constant for the elastomer and skin interface, and a and b are the dimensions of the circuit that define the moment arm distance of the spring force, which correspond to the directional displacement terms (θ_x, θ_y, z). The $[K]$ matrix has canceled off-

https://doi.org/10.1021/acsaelm.1c01107
ACS Appl. Electron. Mater. 2022, 4, 503−512

diagonal terms from the assumption that all spring constants are equal.

Elastomer Spring Constant. We followed a method from Frankovich[38] to calculate the spring constant of the elastomer beneath the circuit. The elastomer and skin were modeled as a rectangular block. The spring constant is found using

$$k = \frac{lwE_{\text{corrected}}}{t}$$

where l, w, and t are the length, width, and thickness of the block and $E_{\text{corrected}}$ is the corrected modulus of the material. For rectangular blocks, this is given by

$$E_{\text{corrected}} = {}^{4}/_{3}E(1 + S^2)$$

where E is the modulus of the material and S is the shape factor, given by

$$S = \frac{\text{area under load}}{\text{area free to bulge}}$$

Substituting the dimensions of the circuit, with an elastomer and skin thickness of 8.8 mm, resulted in an equivalent spring value of 318 N/m.

Strain Layer Modulus. The strain layer was laser cut from solid Mylar sheets, sometimes referred to as biaxially oriented polyethylene terephthalate (boPET). We cut rectangular testing samples, clamped one end, and used a Mark-10 force gauge to apply a displacement at the end. The force vs displacement data was used to solve for the Young's modulus for the cantilever beam with point-force at the end, given by[39]

$$E = \left(\frac{P}{\delta}\right)\frac{4L^3}{bh^3}$$

where $\left(\frac{P}{\delta}\right)$ is the measured value from the bending test and determined by a linear least-squares fit of the data, L is the beam length, b is the beam width, and h is the height. The testing setup and plots of the data are shown in Figure S5. The results were averaged over three trials of specimens with dimensions L = 27.50 mm, b = 19.98 mm, and h = 0.2794 mm, for an elastic modulus value of 4.85 GPa.

Strain Layer Geometry. We adjusted the SIL geometry to reduce the total area of skin restricted by the device. Our previous calculations focused on finding appropriate sheet thicknesses of material to serve as the SIL. Since then, we adjusted our modeling to determine the minimum and maximum feature width of the SIL for our selected sheets of mylar, which are 0.2794 mm (11 mils) thick. Using principal mechanics equations,[39] we find the minimum width for a simply supported rectangular beam by

$$w_{\text{min}} = \sqrt[3]{\frac{PL^3}{4\delta Et}}$$

where w_{min} is the minimum width of the SIL capable of reducing the strain for a given load, P is the force, L is the length, δ is the deflection, E is the elastic modulus, and t is the thickness.

The maximum width capable of still bending to maintain contact with a specified radius of curvature is found by

$$w_{\text{max}} = \frac{5qL^4}{32\delta Et^3}$$

where q is the distributed load of the adhesive force per length of the elastomer holding the SIL in place and all other terms as defined above. In this case, δ can be related to the radius of curvature by

$$\delta = r[1 - \cos({}^{L}/_{2r})]$$

We found values of w_{min} = 2.0 mm and w_{max} = 3.4 mm. We chose a width of 3 mm to further test with FEA and validate through material testing. Actual values for calculation are P = 1 N, L = 21 mm, δ = 0.21 mm (1% strain of the SIL length), E = 4.85 GPa, t = 0.2794 mm, q = 18.32 N/m, and r = 35 mm.

Stretchable Connector Fabrication. We used a flexible tape, made from polyimide (PI), to laminate both sides of a 20 μm thick copper foil. Samples were laser cut using the OPTEC femtosecond laser. The top layer of PI was laser etched to reveal connector pads. The residue was cleaned using acetone and a swab. Then, the outer dimensions of the serpentine were laser cut through all layers. These steps and samples are shown in Figure S7. The etching process used the hatch function in OptiCAD software with the following settings. Hatch style = lines; hatch pitch = 0.01; laser speed = 50; jump speed = 100; laser power = 30; burst time = 1000; repetitions = 0.

Breathable Elastomer Fabrication. The mold used to cure the substrates is shown in Figure S9a as the elastomer is removed from the microneedle array. We maintain a smooth section for the electrode to mount on so that the perforations do not interfere with electrode contact. The dimensions and spacing of the needles (Figure S9b) were used to determine the permeability of the substrate. This is calculated for a unit square area shown as a dashed line. The tapered needles create cone-shaped perforations, and the permeability is a function of the needle spacing and layer height (Figure S9c). We fabricated substrates 0.5 mm thick with a permeability of 7%.

FEA Study. For the FEA study, commercial software COMSOL was used to validate analytical calculations and optimize mechanical performance. The two main components considered were the elastomer substrate and the strain isolation layer. We placed one edge of the elastomer (dimensions 50 × 50 × 0.5 mm^3) as a fixed boundary and prescribed a displacement of 5 mm for the opposite edge. All components were meshed with normal tetrahedral settings for the feature dimensions. The elastomer substrate was modeled as a hyperelastic Neo-Hooke material with Lame parameters λ = 3.88E + 05 and μ = 4.31E + 04. The elastic modulus (E) and Poisson ratio (ν) are E_{SIL} = 4.85 GPa and ν_{SIL} = 0.38.

Study with Human Subjects. The study involved volunteers aged 18−40, and the study was conducted by following the approved IRB protocol (#H17212). Before the in vivo study, all subjects agreed with the study procedures and provided signed consent forms.

■ ASSOCIATED CONTENT

Supporting Information

The Supporting Information is available free of charge at https://pubs.acs.org/doi/10.1021/acsaelm.1c01107.

SIS assembly; vibrational modeling; strain isolation stretch test; strain isolation and device stretch test; SIL material characterization; connector stretch test in elastomer; stretchable connector fabrication; breathability comparison after activity; breathable elastomer mold design and performance (PDF)

Movie S1. Sources of noise (MP4)

Movie S2. Strain layer comparison (MP4)

Movie S3. Breathability test (MP4)

■ AUTHOR INFORMATION

Corresponding Author

Woon-Hong Yeo − *Center for Human-Centric Interfaces and Engineering, Institute for Electronics and Nanotechnology, Georgia Institute of Technology, Atlanta, Georgia 30332, United States; George W. Woodruff School of Mechanical Engineering, Wallace H. Coulter Department of Biomedical Engineering, and Parker H. Petit Institute for Bioengineering and Biosciences, Neural Engineering Center, Institute for Materials, Institute for Robotics and Intelligent Machines, Georgia Institute of Technology, Atlanta, Georgia 30332, United States;* orcid.org/0000-0002-5526-3882; Email: whyeo@gatech.edu

https://doi.org/10.1021/acsaelm.1c01107
ACS Appl. Electron. Mater. 2022, 4, 503−512

Authors

Nathan Rodeheaver − *Center for Human-Centric Interfaces and Engineering, Institute for Electronics and Nanotechnology, Georgia Institute of Technology, Atlanta, Georgia 30332, United States; George W. Woodruff School of Mechanical Engineering, Georgia Institute of Technology, Atlanta, Georgia 30332, United States*

Hojoong Kim − *Center for Human-Centric Interfaces and Engineering, Institute for Electronics and Nanotechnology, Georgia Institute of Technology, Atlanta, Georgia 30332, United States; George W. Woodruff School of Mechanical Engineering, Georgia Institute of Technology, Atlanta, Georgia 30332, United States*

Robert Herbert − *Center for Human-Centric Interfaces and Engineering, Institute for Electronics and Nanotechnology, Georgia Institute of Technology, Atlanta, Georgia 30332, United States; George W. Woodruff School of Mechanical Engineering, Georgia Institute of Technology, Atlanta, Georgia 30332, United States*

Hojin Seo − *Center for Human-Centric Interfaces and Engineering, Institute for Electronics and Nanotechnology, Georgia Institute of Technology, Atlanta, Georgia 30332, United States; George W. Woodruff School of Mechanical Engineering, Georgia Institute of Technology, Atlanta, Georgia 30332, United States;* orcid.org/0000-0002-5715-3193

Complete contact information is available at: https://pubs.acs.org/10.1021/acsaelm.1c01107

Author Contributions

N.R. and W.-H.Y. conceived and designed the research. N.R., H.K., R.H., and H.S. performed the experiments. N.R. and W.-H.Y. analyzed the data. N.R. performed the analytical study and computational modeling. H.S. produced the illustrations and edited the figures. N.R. and W.-H.Y. wrote the paper.

Notes

The authors declare the following competing financial interest(s): Georgia Tech has a pending US patent application related to the work described here.

The data that support the plots within this paper and other findings of this study are available from the corresponding authors upon reasonable request.

■ ACKNOWLEDGMENTS

This work was supported by the Center Grant from the Georgia Tech Institute for Electronics and Nanotechnology and the National Science Foundation/the Centers for Disease Control and Prevention (grant NRI-2024742). Electronic devices in this work were fabricated at the Institute for Electronics and Nanotechnology, a member of the National Nanotechnology Coordinated Infrastructure, which is supported by the National Science Foundation (grant ECCS-2025462).

■ REFERENCES

(1) Matthew, R.; Dutta, J.; Maheswar, R.; Ahmed, K. Intelligent Wearable Electronics: A New Paradigm in Smart Electronics. *Challenges and Solutions for Sustainable Smart City Development* **2021**, 169−197.

(2) Statista Research Department. Estimated growth rates for the global electronics industry from 2019 to 2021, by region. https://www.statista.com/statistics/268396/estimated-growth-rates-for-the-electronics-industry-by-region/ (accessed August 19, 2021).

(3) U.S. Food & Drug Administration. Remote or Wearable Patient Monitoring Devices EUAs. https://www.fda.gov/medical-devices/coronavirus-disease-2019-covid-19-emergency-use-authorizations-medical-devices/remote-or-wearable-patient-monitoring-devices-euas (accessed August 19, 2021).

(4) Gerke, S.; Shachar, C.; Chai, P. R.; Cohen, I. G. Regulatory, safety, and privacy concerns of home monitoring technologies during COVID-19. *Nat. Med.* **2020**, *26* (8), 1176−1182.

(5) He, C. L.; Liang, F. C.; Veeramuthu, L.; Cho, C. J.; Benas, J. S.; Tzeng, Y. R.; Tseng, Y. L.; Chen, W. C.; Rwei, A.; Kuo, C. C. Super Tough and Spontaneous Water-Assisted Autonomous Self-Healing Elastomer for Underwater Wearable Electronics. *Adv. Sci.* **2021**, *8* (21), 2102275.

(6) Liang, F.-C.; Ku, H.-J.; Cho, C.-J.; Chen, W.-C.; Lee, W.-Y.; Chen, W.-C.; Rwei, S.-P.; Borsali, R.; Kuo, C.-C. An intrinsically stretchable and ultrasensitive nanofiber-based resistive pressure sensor for wearable electronics. *J. Mater. Chem. C* **2020**, *8* (16), 5361−5369.

(7) Kim, S. H.; Baek, G. W.; Yoon, J.; Seo, S.; Park, J.; Hahm, D.; Chang, J. H.; Seong, D.; Seo, H.; Oh, S.; Kim, K.; Jung, H.; Oh, Y.; Baac, H. W.; Alimkhanuly, B.; Bae, W. K.; Lee, S.; Lee, M.; Kwak, J.; Park, J. H.; Son, D. A Bioinspired Stretchable Sensory-Neuromorphic System. *Adv. Mater.* **2021**, *33* (44), 2104690.

(8) Kim, K. K.; Choi, J.; Kim, J. H.; Nam, S.; Ko, S. H. Evolvable Skin Electronics by In Situ and In Operando Adaptation. *Adv. Funct. Mater.* **2021**, 2106329.

(9) Venkatesan, M.; Chen, W.-C.; Cho, C.-J.; Veeramuthu, L.; Chen, L.-G.; Li, K.-Y.; Tsai, M.-L.; Lai, Y.-C.; Lee, W.-Y.; Chen, W.-C.; Kuo, C.-C. Enhanced piezoelectric and photocatalytic performance of flexible energy harvester based on CsZn0.75Pb0.25I3/CNC-PVDF composite nanofibers. *Chem. Eng. J.* **2021**, 133620.

(10) Qin, Z.; Lv, Y.; Fang, X.; Zhao, B.; Niu, F.; Min, L.; Pan, K. Ultralight polypyrrole crosslinked nanofiber aerogel for highly sensitive piezoresistive sensor. *Chem. Eng. J.* **2022**, *427*, 131650.

(11) Heikenfeld, J.; Jajack, A.; Rogers, J.; Gutruf, P.; Tian, L.; Pan, T.; Li, R.; Khine, M.; Kim, J.; Wang, J.; Kim, J. Wearable sensors: Modalities, challenges, and prospects. *Lab Chip* **2018**, *18*, 217−248.

(12) Liu, Y.; Norton, J. J. S.; Qazi, R.; Zou, Z.; Ammann, K. R.; Liu, H.; Yan, L.; Tran, P. L.; Jang, K.-I.; Lee, J. W.; Zhang, D.; Kilian, K. A.; Jung, S. H.; Bretl, T.; Xiao, J.; Slepian, M. J.; Huang, Y.; Jeong, J.-W.; Rogers, J. A. Epidermal mechano-acoustic sensing electronics for cardiovascular diagnostics and human-machine interfaces. *Sci. Adv.* **2016**, *2* (11), No. e1601185.

(13) Lee, K.; Ni, X.; Lee, J. Y.; Arafa, H.; Pe, D. J.; Xu, S.; Avila, R.; Irie, M.; Lee, J. H.; Easterlin, R. L.; Kim, D. H.; Chung, H. U.; Olabisi, O. O.; Getaneh, S.; Chung, E.; Hill, M.; Bell, J.; Jang, H.; Liu, C.; Park, J. B.; Kim, J.; Kim, S. B.; Mehta, S.; Pharr, M.; Tzavelis, A.; Reeder, J. T.; Huang, I.; Deng, Y.; Xie, Z.; Davies, C. R.; Huang, Y.; Rogers, J. A. Mechano-acoustic sensing of physiological processes and body motions via a soft wireless device placed at the suprasternal notch. *Nat. Biomed. Eng.* **2020**, *4* (2), 148−158.

(14) Panchal, R.; Horton, L.; Poozesh, P.; Baqersad, J.; Nasiriavanaki, M. Vibration analysis of healthy skin: toward a noninvasive skin diagnosis methodology. *J. Biomed. Opt.* **2019**, *24* (01), 1−1.

(15) Chung, H. U.; Rwei, A. Y.; Hourlier-Fargette, A.; Xu, S.; Lee, K. H.; Dunne, E. C.; Xie, Z.; Liu, C.; Carlini, A.; Kim, D. H.; Ryu, D.; Kulikova, E.; Cao, J.; Odland, I. C.; Fields, K. B.; Hopkins, B.; Banks, A.; Ogle, C.; Grande, D.; Park, J. B.; Kim, J.; Irie, M.; Jang, H.; Lee, J. H.; Park, Y.; Kim, J.; Jo, H. H.; Hahm, H.; Avila, R.; Xu, Y.; Namkoong, M.; Kwak, J. W.; Suen, E.; Paulus, M. A.; Kim, R. J.; Parsons, B. V.; Human, K. A.; Kim, S. S.; Patel, M.; Reuther, W.; Kim, H. S.; Lee, S. H.; Leedle, J. D.; Yun, Y.; Rigali, S.; Son, T.; Jung, I.; Arafa, H.; Soundararajan, V. R.; Ollech, A.; Shukla, A.; Bradley, A.; Schau, M.; Rand, C. M.; Marsillio, L. E.; Harris, Z. L.; Huang, Y.; Hamvas, A.; Paller, A. S.; Weese-Mayer, D. E.; Lee, J. Y.; Rogers, J. A. Skin-interfaced biosensors for advanced wireless physiological monitoring in neonatal and pediatric intensive-care units. *Nat. Med.* **2020**, *26* (3), 418−429.

(16) Kim, Y.-S.; Mahmood, M.; Lee, Y.; Kim, N. K.; Kwon, S.; Herbert, R.; Kim, D.; Cho, H. C.; Yeo, W.-H. All-in-One, Wireless, Stretchable Hybrid Electronics for Smart, Connected, and Ambulatory Physiological Monitoring. *Adv. Sci.* **2019**, *6* (17), 1900939.
(17) Chung, H. U.; Kim, B. H.; Lee, J. Y.; Lee, J.; Xie, Z.; Ibler, E. M.; Lee, K. H.; Banks, A.; Jeong, J. Y.; Kim, J.; Ogle, C.; Grande, D.; Yu, Y.; Jang, H.; Assem, P.; Ryu, D.; Kwak, J. W.; Namkoong, M.; Park, J. B.; Lee, Y.; Kim, D. H.; Ryu, A.; Jeong, J.; You, K.; Ji, B.; Liu, Z.; Huo, Q.; Feng, X.; Deng, Y.; Xu, Y.; Jang, K. I.; Kim, J.; Zhang, Y.; Ghaffari, R.; Rand, C. M.; Schau, M.; Hamvas, A.; Weese-Mayer, D. E.; Huang, Y.; Lee, S. M.; Lee, C. H.; Shanbhag, N. R.; Paller, A. S.; Xu, S.; Rogers, J. A. Binodal, wireless epidermal electronic systems with in-sensor analytics for neonatal intensive care. *Science* **2019**, *363* (6430), eaau0780.
(18) Lin, R.; Li, Y.; Mao, X.; Zhou, W.; Liu, R. Hybrid 3D Printing All-in-One Heterogenous Rigidity Assemblies for Soft Electronics. *Adv. Mater. Technol.* **2019**, *4* (12), 1900614.
(19) Zhang, Z.; Silva, I.; Wu, D.; Zheng, J.; Wu, H.; Wang, W. Adaptive motion artefact reduction in respiration and ECG signals for wearable healthcare monitoring systems. *Med. Biol. Eng. Comput.* **2014**, *52* (12), 1019−1030.
(20) Jeong, J. W.; Yeo, W. H.; Akhtar, A.; Norton, J. J. S.; Kwack, Y. J.; Li, S.; Jung, S. Y.; Su, Y.; Lee, W.; Xia, J.; Cheng, H.; Huang, Y.; Choi, W. S.; Bretl, T.; Rogers, J. A. Materials and optimized designs for human-machine interfaces via epidermal electronics. *Adv. Mater.* **2013**, *25* (47), 6839−6846.
(21) Kwon, Y.-T.; Kim, Y.-S.; Kwon, S.; Mahmood, M.; Lim, H.-R.; Park, S.-W.; Kang, S.-O.; Choi, J. J.; Herbert, R.; Jang, Y. C. All-printed nanomembrane wireless bioelectronics using a biocompatible solderable graphene for multimodal human-machine interfaces. *Nat. Commun.* **2020**, *11* (1), 3450.
(22) Kim, H.; Kim, Y. S.; Mahmood, M.; Kwon, S.; Zavanelli, N.; Kim, H. S.; Rim, Y. S.; Epps, F.; Yeo, W. H. Fully Integrated, Stretchable, Wireless Skin-Conformal Bioelectronics for Continuous Stress Monitoring in Daily Life. *Adv. Sci.* **2020**, *7* (15), 2000810.
(23) Tian, L.; Zimmerman, B.; Akhtar, A.; Yu, K. J.; Moore, M.; Wu, J.; Larsen, R. J.; Lee, J. W.; Li, J.; Liu, Y.; Metzger, B.; Qu, S.; Guo, X.; Mathewson, K. E.; Fan, J. A.; Cornman, J.; Fatina, M.; Xie, Z.; Ma, Y.; Zhang, J.; Zhang, Y.; Dolcos, F.; Fabiani, M.; Gratton, G.; Bretl, T.; Hargrove, L. J.; Braun, P. V.; Huang, Y.; Rogers, J. A. Large-area MRI-compatible epidermal electronic interfaces for prosthetic control and cognitive monitoring. *Nat. Biomed. Eng.* **2019**, *3* (3), 194−205.
(24) Huigen, E.; Peper, A.; Grimbergen, C. A. Investigation into the origin of the noise of surface electrodes. *Med. Biol. Eng. Comput.* **2002**, *40*, 332−338.
(25) Gleskova, H.; Wagner, S.; Suo, Z. a-Si:H thin film transistors after very high strain. *J. Non-Cryst. Solids* **2000**, *266*−*269*, 1320−1324.
(26) Park, S.-I.; Ahn, J.-H.; Feng, X.; Wang, S.; Huang, Y.; Rogers, J. A. Theoretical and Experimental Studies of Bending of Inorganic Electronic Materials on Plastic Substrates. *Adv. Funct. Mater.* **2008**, *18* (18), 2673−2684.
(27) Umar, A. H.; Othman, M. A.; Harun, F. K. C.; Yusof, Y. Dielectrics for Non-contact ECG Bioelectrodes: A Review. *IEEE Sens. J.* **2021**, *21*, 18353.
(28) Prasad, A. S; Jayaram, M N; Swamy N, K. Fabrication of GNR Electrode for ECG signal acquisition. *IEEE Sens. Lett.* **2021**, *5*, 1.
(29) Porr, B.; Howell, L. R-peak detector stress test with a new noisy ECG database reveals significant performance differences amongst popular detectors. 2019, bioRxiv. https://www.biorxiv.org/content/10.1101/722397v3.
(30) *MAX-ECG-MONITOR User Guide*; **2018**; p 15.
(31) Barrett, P. M.; Komatireddy, R.; Haaser, S.; Topol, S.; Sheard, J.; Encinas, J.; Fought, A. J.; Topol, E. J. Comparison of 24-h Holter monitoring with 14-day novel adhesive patch electrocardiographic monitoring. *Am. J. Med.* **2014**, *127* (1), 95.e11−95.e17.
(32) Rho, R.; Vossler, M.; Blancher, S.; Poole, J. E. Comparison of 2 ambulatory patch ECG monitors: The benefit of the P-wave and signal clarity. *Am. Heart J.* **2018**, *203*, 109−117.
(33) Nault, I.; Andre, P.; Plourde, B.; Leclerc, F.; Sarrazin, J. F.; Philippon, F.; O'Hara, G.; Molin, F.; Steinberg, C.; Roy, K.; Blier, L.; Champagne, J. Validation of a novel single lead ambulatory ECG monitor - Cardiostat - Compared to a standard ECG Holter monitoring. *J. Electrocardiol.* **2019**, *53*, 57−63.
(34) Upadhyayula, S.; Kasliwal, R. Wellysis S-PAtch Cardio versus Conventional Holter Ambulatory Electrocardiographic Monitoring (The PACER Trial): Preliminary Results. *Journal of Clinical and Preventive Cardiology* **2019**, *8* (4), 173−173.
(35) Walsh, J. A.; Topol, E. J.; Steinhubl, S. R. Novel wireless devices for cardiac monitoring. *Circulation* **2014**, *130* (7), 573−581.
(36) Rodeheaver, N.; Herbert, R.; Kim, Y. S.; Mahmood, M.; Kim, H.; Jeong, J. W.; Yeo, W. H. Strain-Isolating Materials and Interfacial Physics for Soft Wearable Bioelectronics and Wireless, Motion Artifact-Controlled Health Monitoring. *Adv. Funct. Mater.* **2021**, *31*, 2104070.
(37) Meirovitch, L. *Fundamentals of Vibrations*; Waveland Press, Inc.: Long Grove, IL, 2010; pp 212−215.
(38) Frankovich, D. *Basics of Vibration Isolation Using Elastomeric Materials*; 2002, pp 2−7.
(39) Goodno, B. J.; Gere, J. M. *Mechanics of materials*, 9th ed.; Cengage: Mason, OH, 2017; pp 416−482.
(40) *VSMS ECG patch − Professional User Guide | Rev EUA*; **2020**; p 42.
(41) Fung, E.; Järvelin, M. R.; Doshi, R. N.; Shinbane, J. S.; Carlson, S. K.; Grazette, L. P.; Chang, P. M.; Sangha, R. S.; Huikuri, H. V.; Peters, N. S. Electrocardiographic patch devices and contemporary wireless cardiac monitoring. *Front. Physiol.* **2015**, *6* (MAY). DOI: 10.3389/fphys.2015.00149
(42) *MiCor A100 Wearable ECG Recorder - User Guide*; **2020**; p 32.

SUPPORTING INFORMATION

Breathable, Wireless, Thin-Film Wearable Biopatch Using Noise-Reduction Mechanisms

Nathan Rodeheaver[a,b], Hojoong Kim[a,b], Robert Herbert[a,b], Hojin Seo[a,b], and Woon-Hong Yeo[a,b,c,d,*]

[a]Center for Human-Centric Interfaces and Engineering, Institute for Electronics and Nanotechnology, Georgia Institute of Technology, Atlanta, GA 30332, USA.
[b]George W. Woodruff School of Mechanical Engineering, Georgia Institute of Technology, Atlanta, GA 30332, USA.
[c]Wallace H. Coulter Department of Biomedical Engineering, Georgia Institute of Technology, Atlanta, GA 30332, USA.
[d]Parker H. Petit Institute for Bioengineering and Biosciences, Neural Engineering Center, Institute for Materials, Institute for Robotics and Intelligent Machines, Georgia Institute of Technology, Atlanta, GA 30332, USA.
*Address correspondence to whyeo@gatech.edu

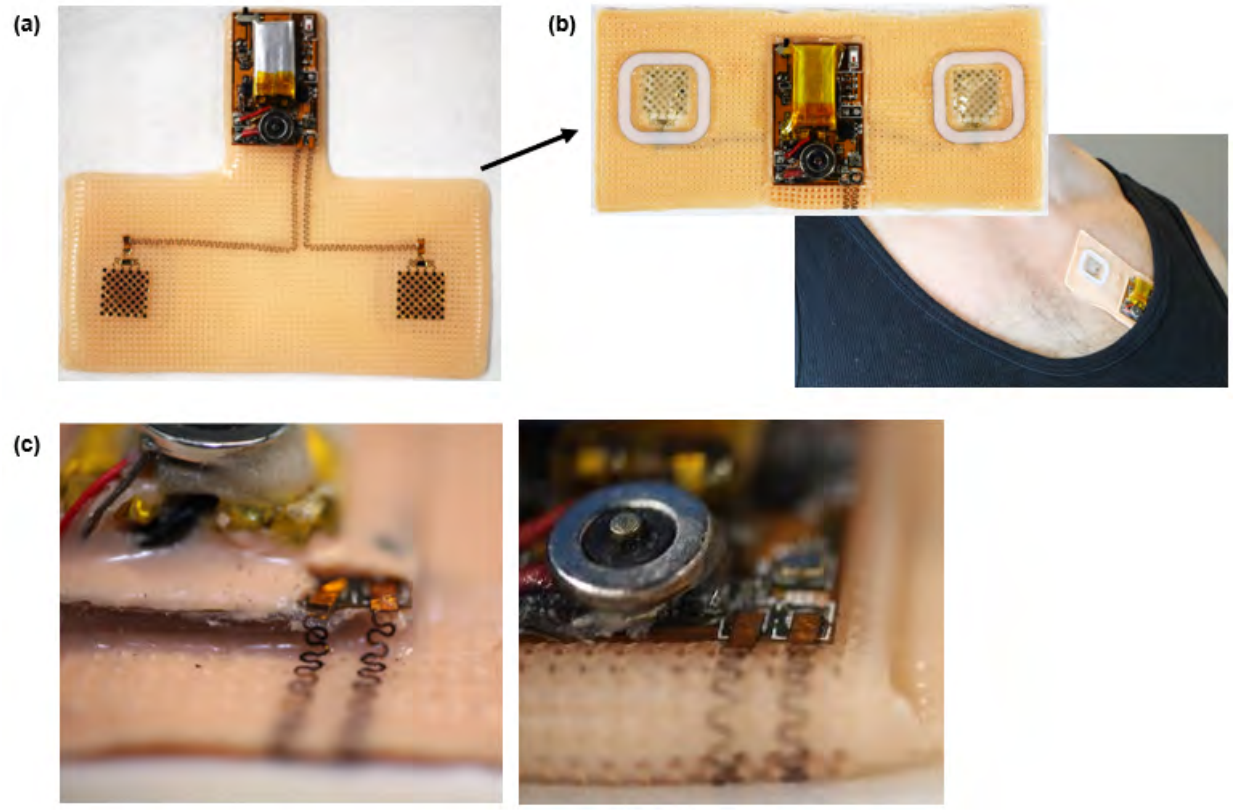

Figure S1. SIS Assembly.
(a) Electrodes, stretchable connections, and fPCB circuit are placed on unfolded elastomer. (b) Elastomer flap with circuit is folded to top and SIL are secured around electrodes. Chest placement of completed device. (c) Comparison of original elastomer design (left) to foldable elastomer design (right). Foldable design reduces connection stretching in the z-direction.

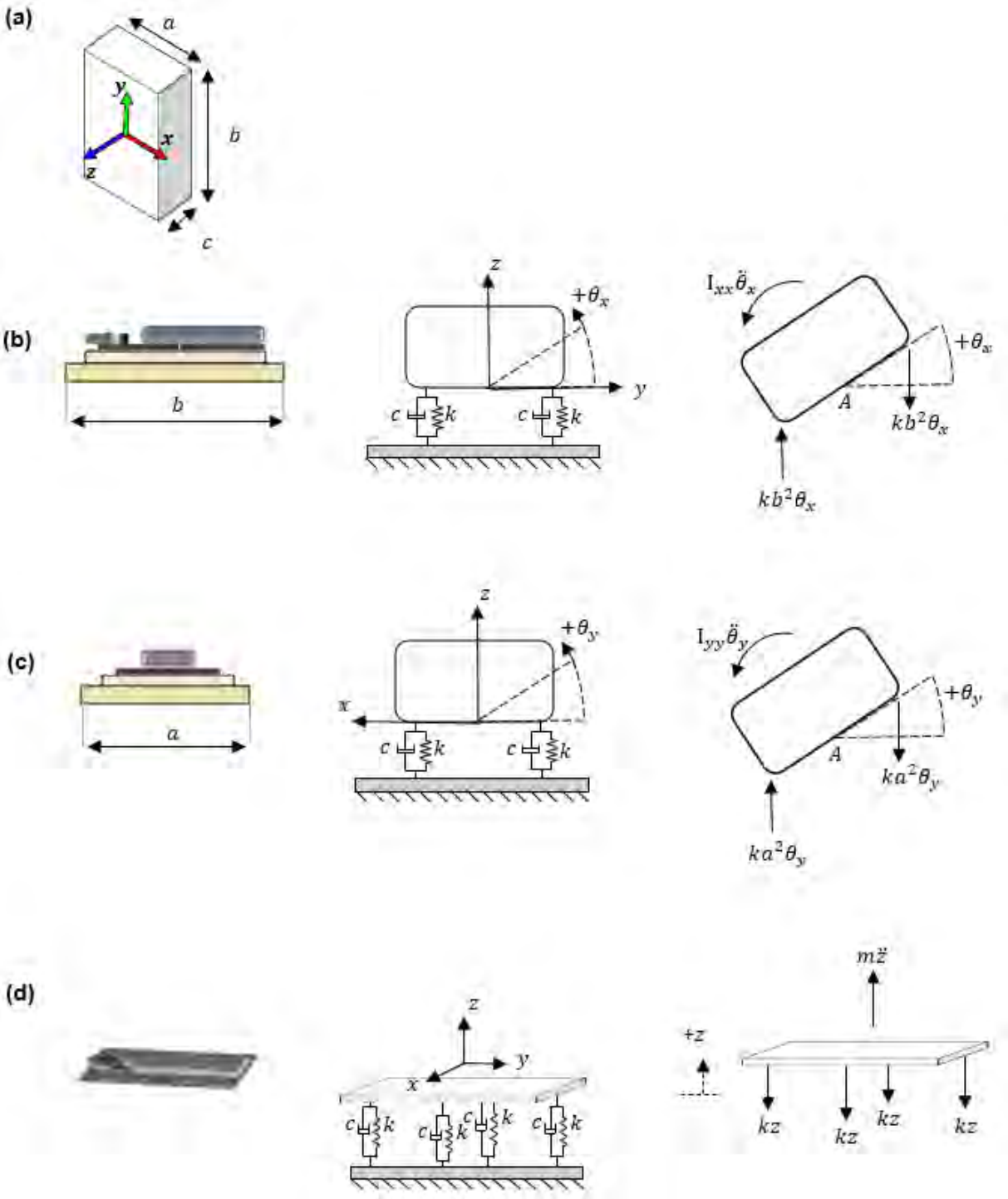

Figure S2. Vibrational modeling.
(a) XYZ orientation and dimensions of rectangular block. (b) Side view (yz-plane) of circuit with mass-spring-damper and free-body-diagram for x-rotation about point A. (c) Top view (xz-plane) of circuit with mass-spring-damper and free-body-diagram for y-rotation about point A. (d) Isometric view of circuit with mass-spring-damper and free-body-diagram for z-translation.

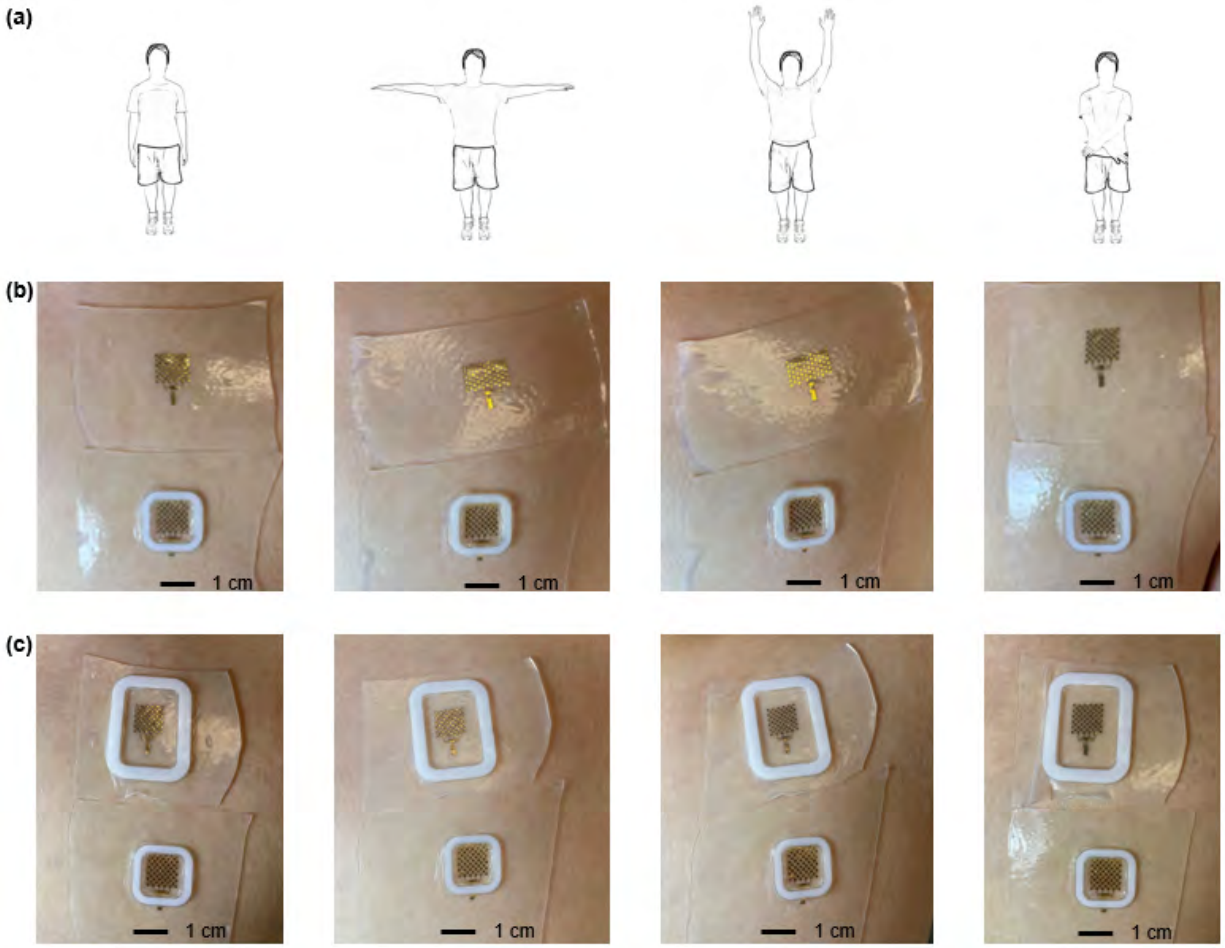

Figure S3. Strain isolation stretch test.
(a) Illustration of arm position for standing with arms at side, arms outstretched, arms overhead, and arms crossed in front of the body. These arm positions correspond, by column, for the following pictures. (b) Pictures of electrodes and elastomer placed on the chest. The top electrode shows significant stretching when arms are outstretched and overhead, while the strain isolation layer shields the bottom electrode. (c) Pictures of two strain isolation layers placed on the chest. Both samples prevent skin strain during tension, but the top sample shows delamination under compression when arms are crossed.

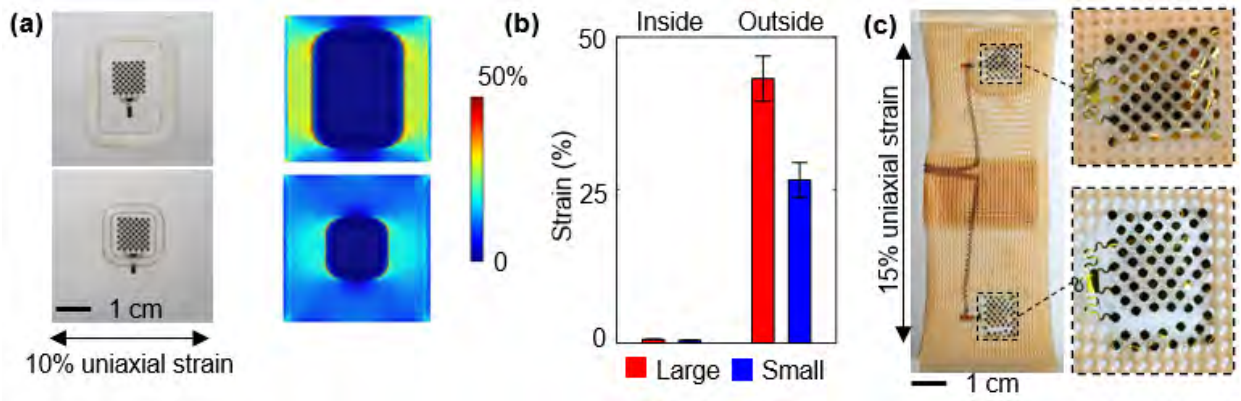

Figure S4. Strain isolation and device stretch test.
(a) FEA of mylar strain isolation layer (SIL) with large and small geometries. (b) Comparison of strain inside and outside the large and small SIL. Mean and standard deviation for n=17 randomly selected measurement locations. (c) Tension results of the entire device showing large strain and electrode damage without SIL.

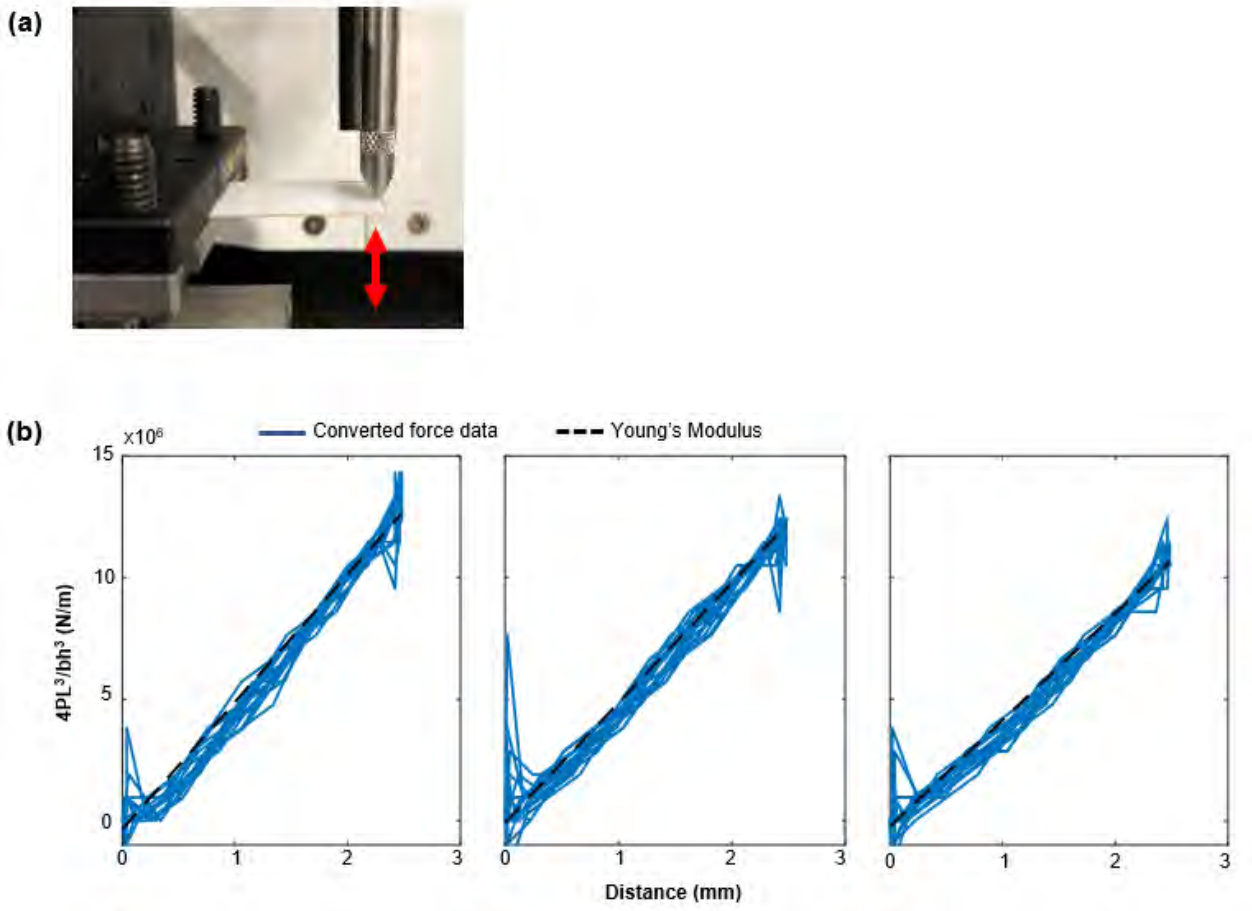

Figure S5. SIL material characterization.
(a) Testing setup with Mark-10 force gauge and mylar sample in cantilever beam configuration with point force at the end of the beam. (b) Results of three trials with linear least-squares fit of slope to calculate Young's modulus. Average of 3 trials= 4.85 GPa.

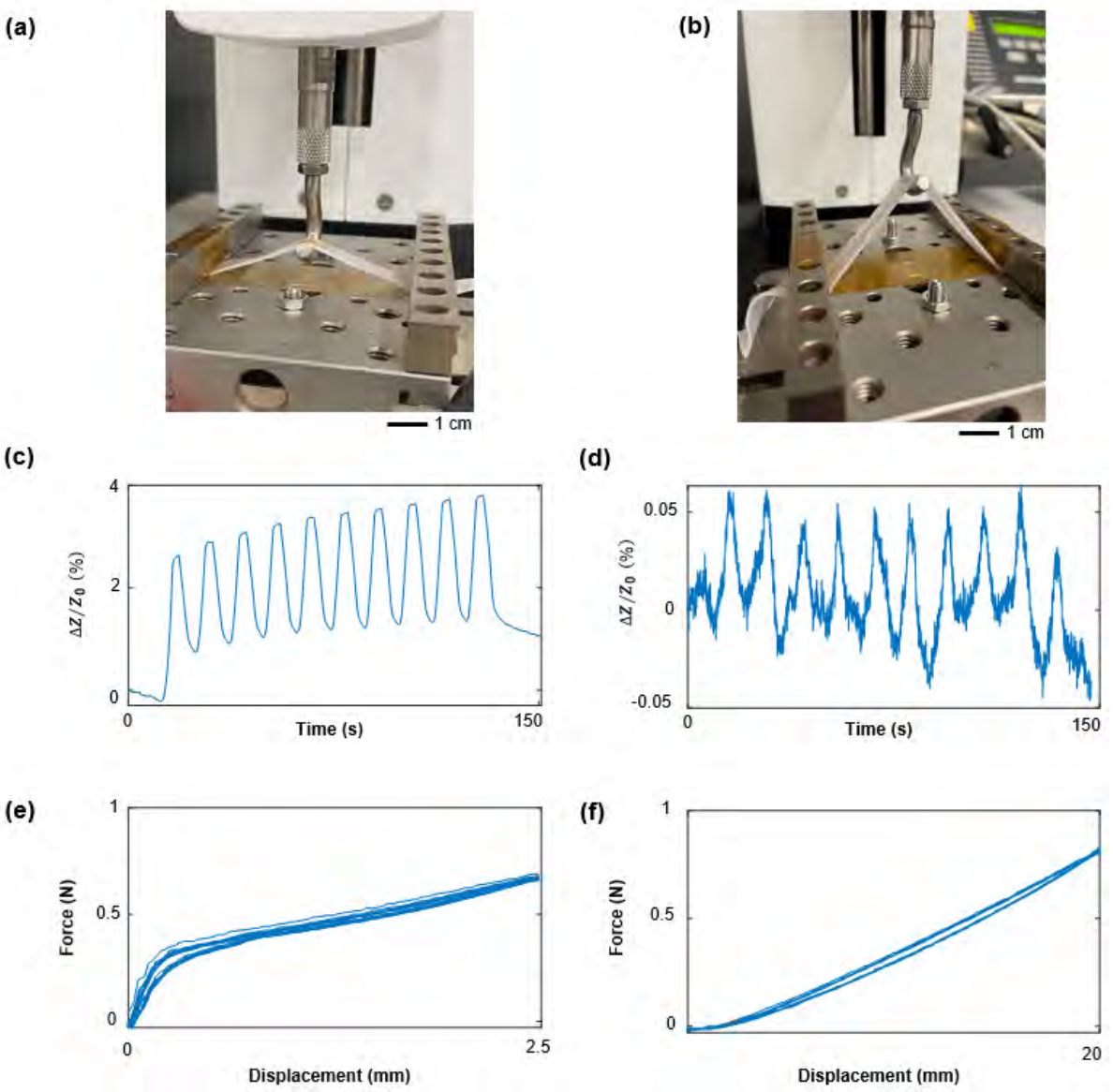

Figure S6. Connector stretch test in an elastomer.
(a,b) Testing setup with Mark-10 force gauge and BK Precision LCR meter. Elastomer was stretched from the middle, with clamps at each end to prevent movement of the LCR meter connection.(a) Flexible connector with 2.5 mm travel. (b) Stretchable connector with 20 mm travel. (c) Impedance change for flexible connector over 10 cycles. (d) Impedance change for stretchable connector over 10 cycles. (e) Force vs. displacement for a flexible connector. (f) Force vs. displacement for a stretchable connector.

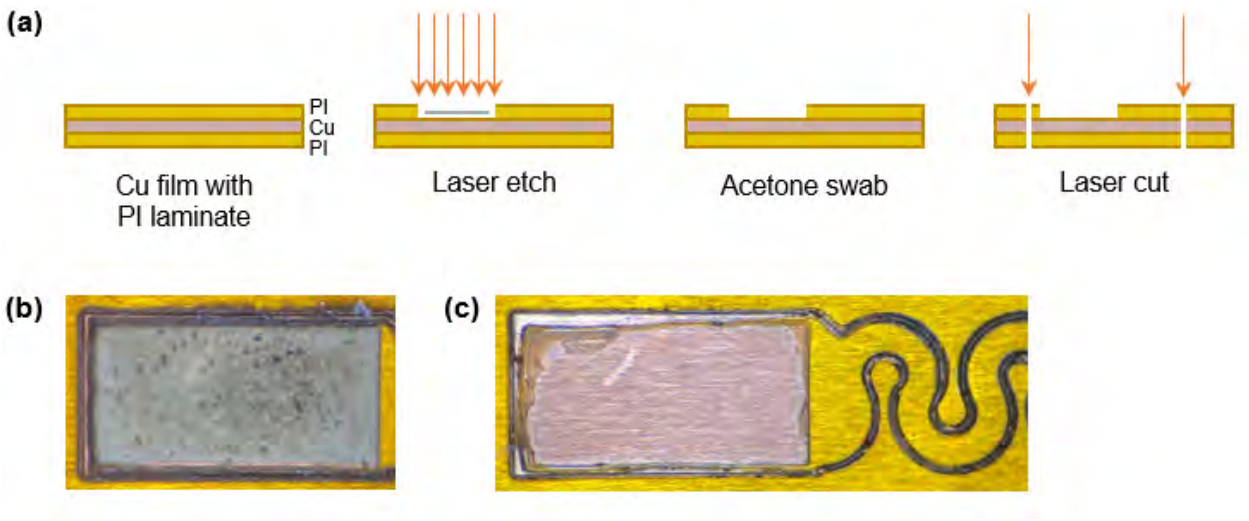

Figure S7. Stretchable connector fabrication.
(a) Fabrication steps of polyimide (PI) insulated copper film. From left to right: starting film, laser etch connector pad through top PI layer, residue removal with acetone and swab, laser cut outer pattern through all layers. (b) Photo of laser-etched PI (gray portion). (c) Cu pad exposed after acetone swab.

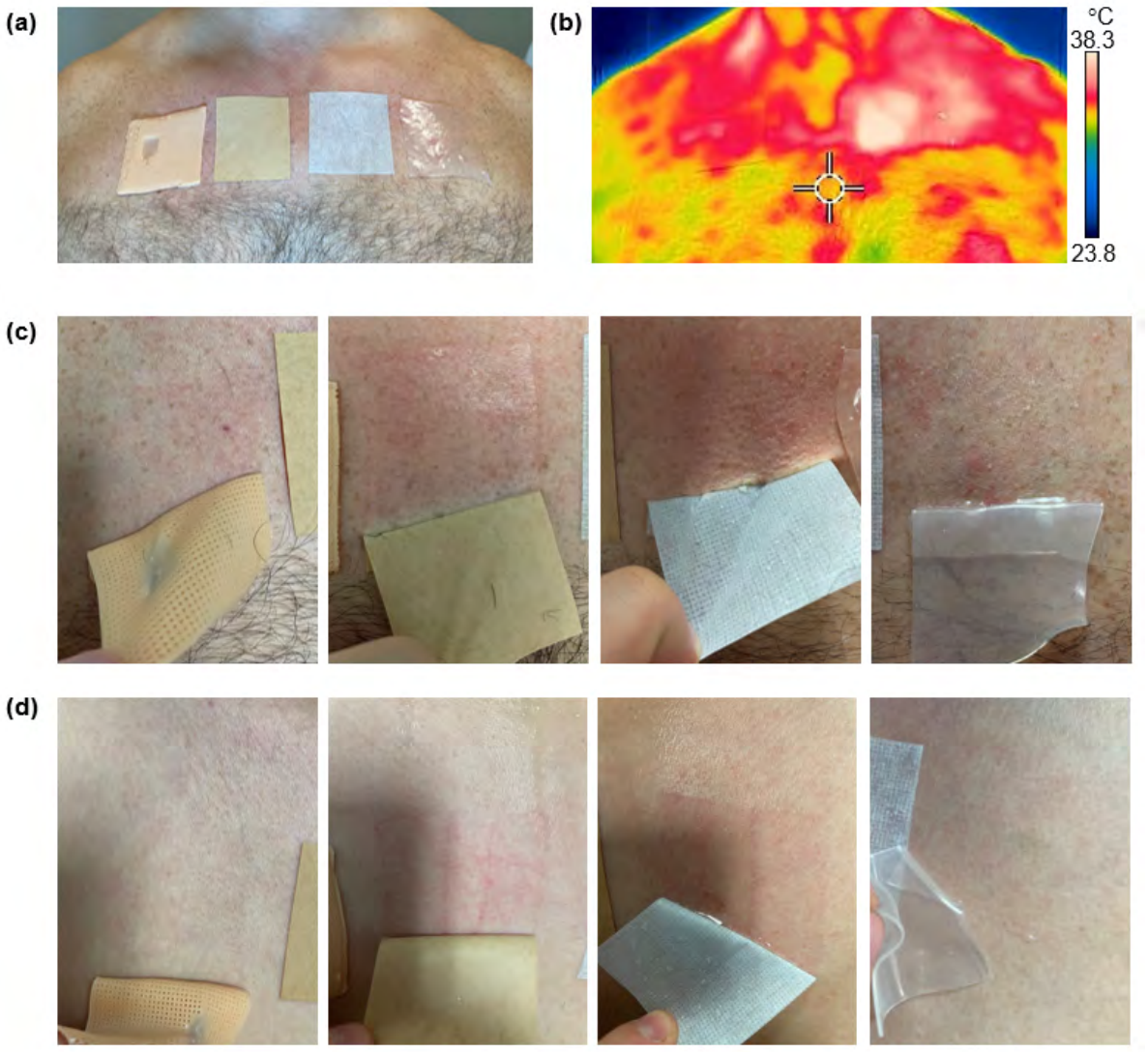

Figure S8. Breathability comparison after activity.
(a) Placement of breathable elastomer, 3M™ Medical Tape 9907T, 3M™ Micropore™ S, and solid elastomer. (b) FLIR temperature results after 20 minutes of walking outside at 32°C temperature. (c) Results for subject 1. (d) Results for subject 2.

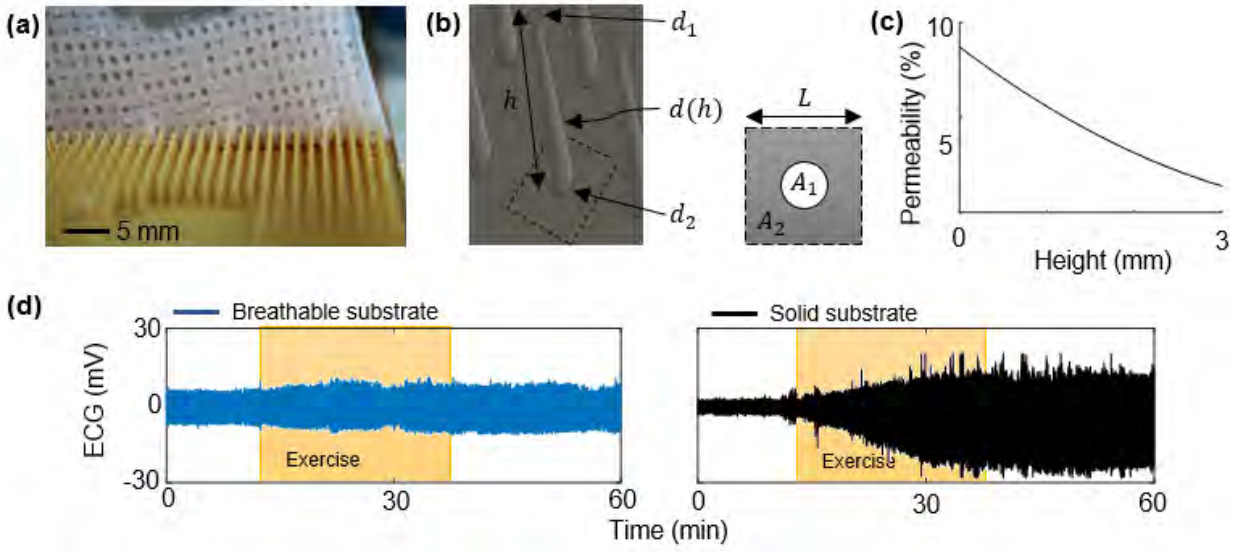

Figure S9. Breathable elastomer mold design and performance.
(a) Breathable substrate fabricated using a mold with a microneedle array. (b) Dimensions of microneedle spacing. (c) Percent of permeability vs. thickness of elastomer. (d) Raw data for ECG comparison from Figure 5.

Table S1. Comparison of motion artifact reduction by activity and design strategy

	Walking	Jogging	Stretching	Hot weather	Long-term recording
Form factor	Yes	Yes	No	No	Yes
Strain isolation	No	Yes	Yes	No	Yes
Stretchable connectors	Yes	Yes	Yes	No	Yes
Breathability	No	Yes	No	Yes	Yes

Movie S1. Sources of noise.
Demonstration of signal noise caused by circuit movement, electrode disturbance, and connection disturbance.

Movie S2. Strain layer comparison.
Performance comparison between large and small SIL for arm motions following the sequence of Figure S3a. SIL's were recorded in each position, where the top position experiences more skin strain. In each case, the larger SIL shows strain concentration along the edge resulting in temporary delamination.

Movie S3. Breathability test for perforated elastomer and commercial tapes.
Performance of commercial tapes, solid elastomer, and perforated elastomer. Each sample was placed with the adhesive side up to mimic moisture flowing from the skin's surface through the sample to the shirt fabric on the other side. Each sample, and the surrounding fabric, was thoroughly wetted with water before testing for equal comparison of the wicking capillary action through the substrate into the shirt fabric. The volume of water from every pipet deposition is 20 ml. The samples were given 60 s to show any water transmission, and the first clips are sped up 8 times. The final clip shows real-time water transmission for the flipped perforated substrate with multiple water deposits.